ORIGINAL ARTICLE

In situ studies of full-field residual stress mapping of SS304 stainless steel welds using DIC

Huabin Chen[1] · Yulin Song[1] · Xiaoqi Chen[2] · Xinghua Yu[3] · Shanben Chen[1]

Abstract

Large tensile residual stress is detrimental to the structural integrity of welded structures. As a result, it is very important to understand the residual formation during the welding process. In this paper, a new non-contact welding residual stress measurement technique based on digital image correlation (DIC) is proposed as a way to investigate residual stress formation. To investigate the stress evolution of the welded plate, we conduct a series of experiments by using this new method. High-temperature full-field strain obtained from DIC was computed by incremental theory to acquire stress increment. Stress evolution and residual stress were obtained by superimposing the stress increment. Hole-drilling residual stress measurements for verification were also implemented. The maximum difference, which was 37 MPa between the two methods demonstrated that this new technique was able to characterize the full-field welding residual stress during the welding process.

Keywords Full-field residual stress · Stress evolution · Digital image correlation · Arc welding · High temperature

1 Introduction

The residual plastic deformation and residual stresses are caused by differential thermal expansion and contraction of the weld and base metal due to the vicinity of welded joints by the localized heating and subsequent cooling of the welded joint. Very often, residual stresses have a significant effect on the properties of materials and structural components, notably bearing capacity, fatigue life, brittle fracture, and stability [1–3]. Residual stresses are detrimental to the fatigue, fracture, and corrosion resistance of welds, which are critical in the design of parts and structural components and in the estimation of their structure integrity [4, 5]. Residual stress measurement plays an important role in understanding and improving the quality of welds. During the past years, many different methods for measuring the residual stress in different types of components have been developed [6]. Hole-drilling is one of the principle semi-destructive techniques used to measure residual stress in the manufactured structure. Its reliability and accuracy strongly depend on the type of the strain gauge and the implementation of measurement [7]. Additionally, methods such as ring-core, deep-hole, and hole-drilling combined with DIC are similar in theory with the hole-drilling method which depends on releasing the stress by removing material to infer the residual stress [8–10]. However, only in a limited number of points can be measured and the final stress state is known in these methods. The contour method is a destructive method which cuts the object into several parts. The stress state of structure cannot be fully reflected since the direction of the stress obtained is simple [11]. The workpiece measured with destructive methods such as contour, multi-contour, and sectioning is destroyed and could not be measured for other purposes. X-ray and neutron diffraction which are non-destructive base on the variations of lattice spacing to infer residual stress [12, 13], such measurements generally require an unstressed reference lattice spacing which is influenced by the composition. However, changes in composition would result in significant errors [14]. For certain applications, these diffraction techniques suffer from serious scatter

✉ Huabin Chen
  hbchen@sjtu.edu.cn

✉ Xiaoqi Chen
  xiaoqichen@swin.edu.au

1 Shanghai Key Laboratory of Materials Laser Processing and Modification, Shanghai Jiao Tong University, Shanghai 200240, People's Republic of China

2 Department of Mechanical and Product Design Engineering, Swinburne University of Technology, Melbourne, Australia

3 School of Materials Science and Engineering, Beijing Institute of Technology, Beijing 100081, People's Republic of China

Table 1 Welding parameter

Welding process number	Layer order	Current (A)	Voltage (V)	Welding speed (mm/s)
I	1	170	13	3
II	1	170	13	3
	2	190	13	3

problems due to the large granular structure, affecting the resolution. Neutron diffraction stress maps have practical limits because the required beam time grows exponentially with the dimensionality of mapping. The components also have to be sent to large central research facilities for the measurements to be taken.

DIC is advantageous in terms of its non-contact full-field measurement nature, and robustness in correlation algorithmic technique has been widely adopted in industries. DIC is a mature technology for strain measurement [15, 16]. Usually, digital images were collected and displacement and strain of subsets in the region of interest (ROI) are acquired by comparing the images in the undeformed and deformed states, respectively. The DIC technique, which relies on cameras and computers, is a full-field non-contact technique. It has a simple set-up and requires less space compared to other measuring methods that make it work in a complex environment. During the past few years, the DIC method has been extensively developed and accuracy in strain measurement has been improved significantly with more and more applications [17, 18]. A comprehensive study on determining the mechanical properties of the weld line including HAZ by the DIC and inverse modeling methodology has been presented. The strain hardening

exponent is first determined by 3D DIC [19]. To calculate the plastic strain ratio through-thickness strain, the DIC technique was used to measure the surface strain field of both micro- and macro-samples and to point out possible inhomogeneities in the plastic behavior of the TWB weld beads [20].

Agarwal et al. [21] reported the in situ strain evolution during a laser welding manufacturing with the DIC method. They concluded that the method can estimate local strain as close as 1.5 mm from the fusion boundary.3D-DIC based on the principle of binocular stereo-vision was developed to measure the 3D deformation which is inapplicable in 2D-DIC. The raise of the high-temperature resist speckle pattern preparation method makes DIC be used for measuring deformation during welding. Even though strain evolution and weld deformation could be measured [22], residual stress development and final residual stress state in the weld still could not be understood. As a result, it is critical to develop a technique to further computer stress from the strain which is measured by the DIC technique.

The DIC method provides a convenient and reliable way to measure strain evolution which could be translated to stress. Due to the limitations of other residual stress measurement techniques mentioned previously, a non-destructive method based on 2D-DIC strain and is proposed to measure full-field residual stress in welded structures in this paper. This technique mainly integrates the strain field obtained by the DIC method and temperature field to compute the corresponding stress during the whole welding process by the material constitutive relationship. The welding residual stress is acquired finally. This technique has the advantage of non-contact and non-destructive, the system is easy to establish, and two-dimensional residual stress can be acquired. This new stress measurement technique also makes it possible for the
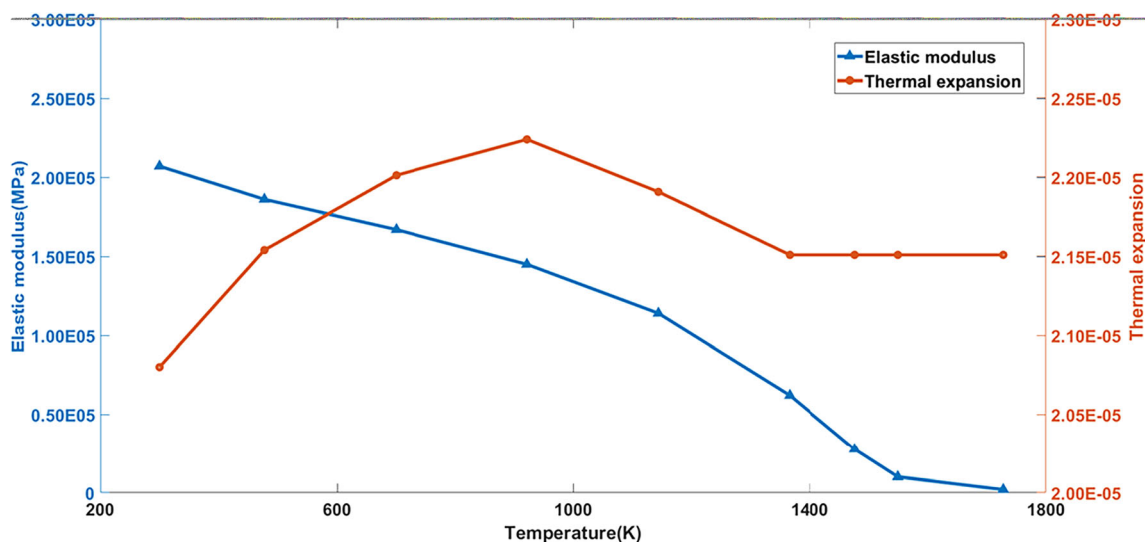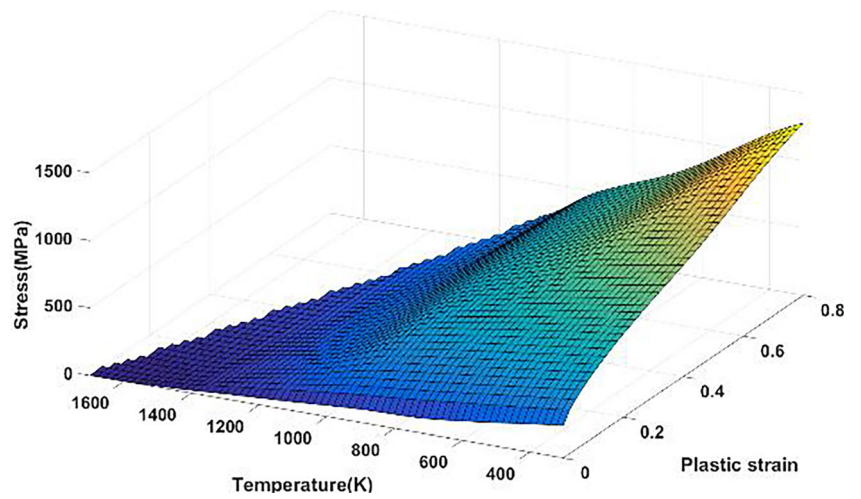

Fig. 1 Temperature-dependent thermophysical and mechanical properties

Fig. 2 Interpolation curve surface of stress

first time to monitor strain and stress evolution during the welding process. The residual stress evolution could be further used as feedback to control residual stress and prevent weld defects.
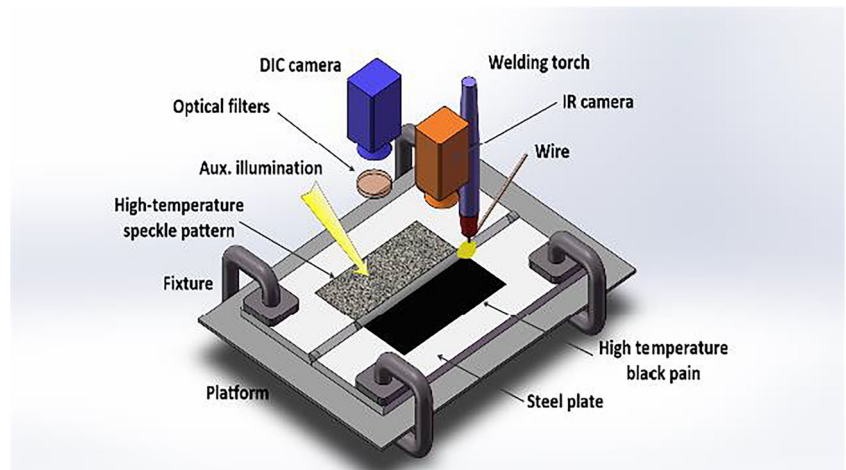
Fig. 3 Experiment set-up

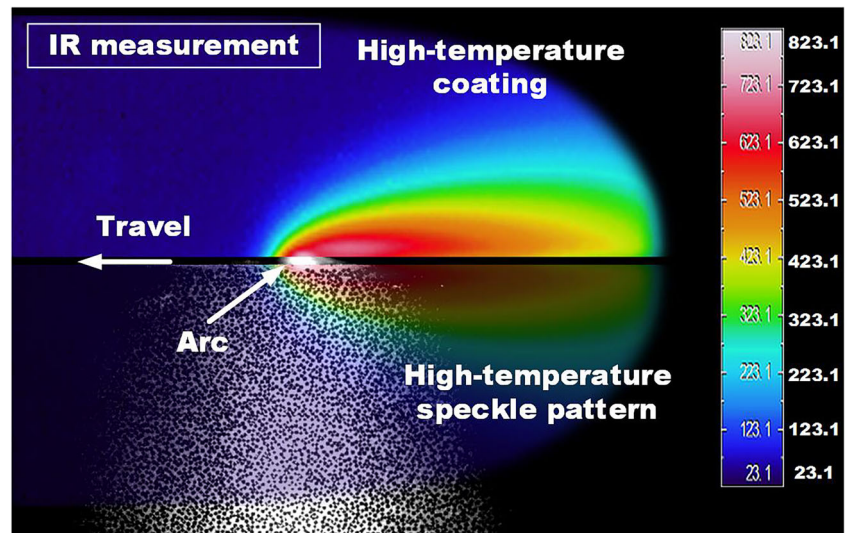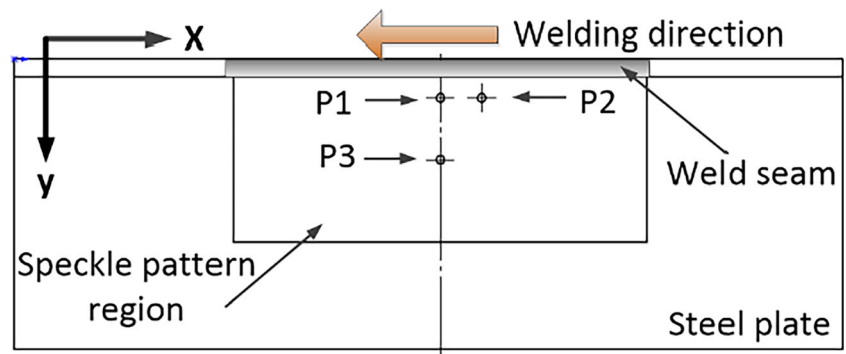**Fig. 4** Temperature distribution at 15 s after arc on (temperature unit is degree Celsius)

Fig. 5 Position of drilling holes

2 Experimental

Two groups of argon shielded tungsten arc welding experiments were performed on Type SS304 stainless plates to get butt welds. The plates were annealed to remove any potential internal stresses. The wire was fed in the front of the weld pool. The seam was composed of one layer in experiment I and two layers in experiment II. The welding parameters are listed in Table 1.

Four clamps were used to fix the plates and two spot welds were produced before the welding process to obtain good weld and reduce the out of plane distortion. The temperature-dependent thermophysical and mechanical properties of the base metal were collected from various sources [23] and showed in Fig. 1, and the plastic strain and corresponding flow stress in different temperatures was interpolated to obtain the curve surface showed in Fig. 2.

A camera was used to record the images of the steel plate surface at 5 frames per second during thermal cycles (down to room temperature after welding). As shown in Fig. 3, the experimental system was equipped with a special designed laser auxiliary illumination and an optical filter, which was utilized to prevent light interference from the arc.

Before welding, a rectangular area on the surface of the steel plate beside the seam was prepared with novel speckle patterns which will survive at elevated temperature during welding by selective oxidization. In order to obtain the temperature evolution during the welding process accurately, a black paint with an emittance of 0.9 was sprayed on the non-speckled plate. An infrared camera was used to record its temperature data. The DIC camera and IR camera fixed on tripods were positioned in the direction perpendicular to the steel plates to measure the in-plane strain and temperature evolution. The image of the temperature filed and corresponding speckle pattern at 15 s after arc on is showed in Fig. 4.

The base metal plate's dimension is 200 mm × 70 mm × 6 mm (length × width × thickness), which is showed in Fig. 5, and the weld seam was about 100 mm long. The speckle pattern region and black paint area were both 100 mm × 40 mm. Residual stress of 3 points (P1 ~ P3) were measured with hole-drilling method in both experiments I and II. The results were compared with the corresponding points' residual stress measured with the method proposed in this paper. The position of P1 ~ P3 is showed in Fig. 5; the distance between P1 and the axis of the weld was 10 mm, P1 and P2 was 10 mm, and P1 and P3 was 15 mm. The hole-drilling measurement following the ASTM-E837–08 standard was made using an annular cutter with a diameter of 2 mm, allowing for stress to be measured up to a depth of about 2 mm. Strain rosettes with an angle of 45° were utilized, and the reference direction was parallel to the axis of the weld (i.e., x) showed in Fig. 5. The least distance among holes was 10 mm which was 5 times the annular cutter's diameter, ensuring that the point residual stress released made no effects on the subsequent

Fig. 6 Full-field strain map during welding at t = 15 s. **a** Strain field along axis x at 15 s; **b** Strain field along axis y at 15 s

(a)
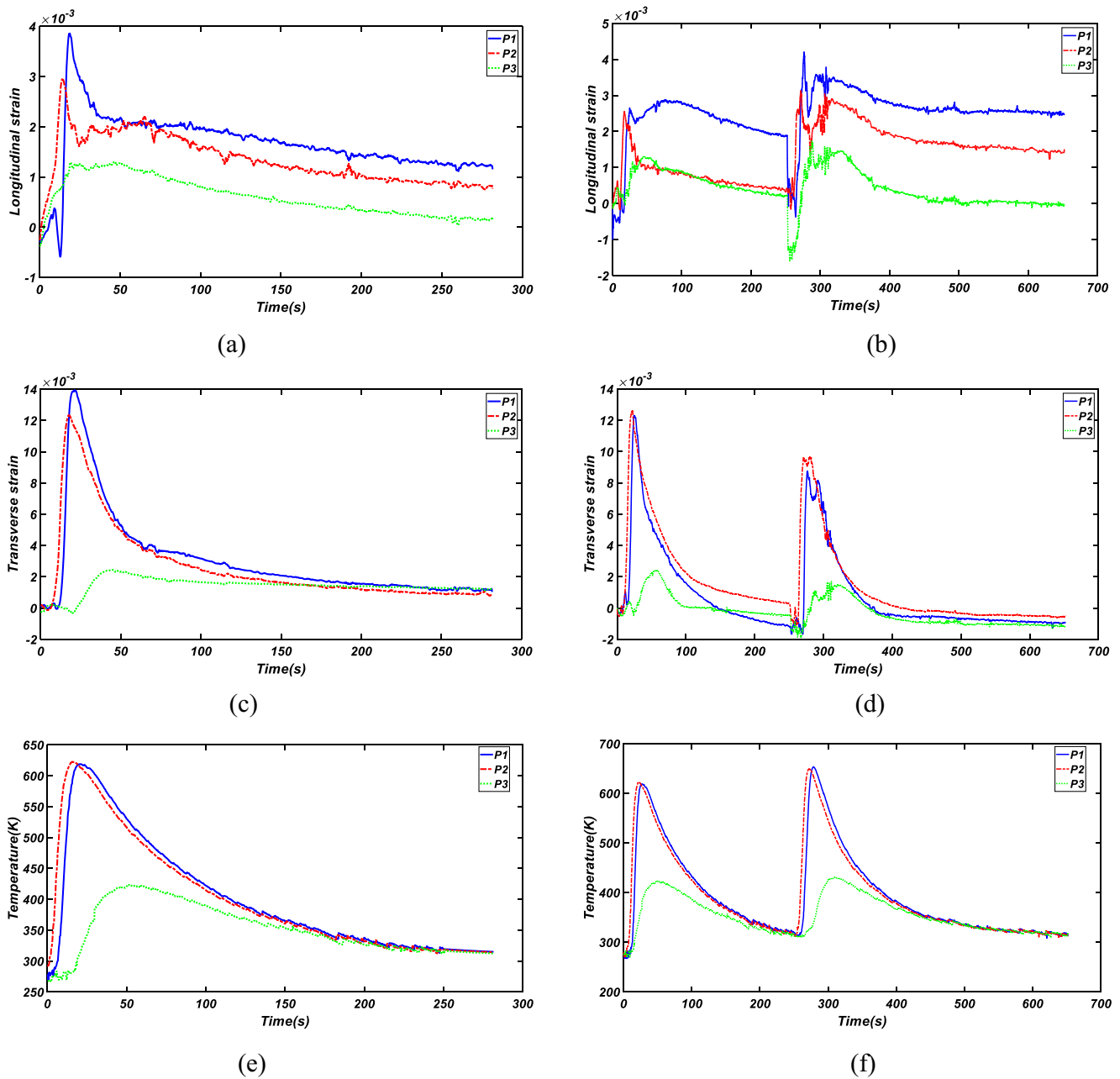

(b)

(a)

(b)

(c)

(d)

(e)

(f)
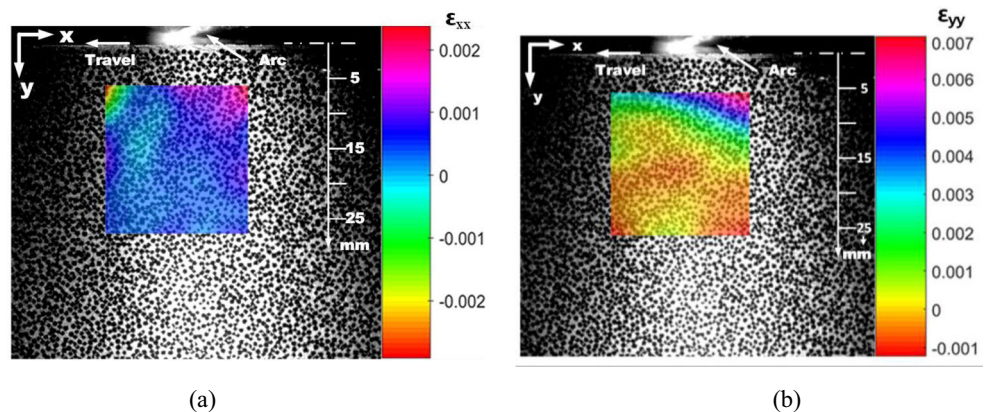
Fig. 7 The strain evolution of P1 ~ P3 in experiments Iand II. **a** Longitudinal strain evolution of P1 ~ P3 in experiment I. **b** Longitudinal strain evolution of P1 ~ P3 in experiment II. **c** Transverse strain evolution of P1 ~ P3 in experiment I. **d** Transverse strain evolution of P1 ~ P3 in experiment II. **e** Temperature evolution of P1 ~ P3 in experiment I. **f** Temperature evolution of P1 ~ P3 in experiment II

ones. A comparison of measurement results with these two different methods is showed in the "Results and discussion" section.

The strain field of a ROI included P1 ~ P3 was calculated after post-processing all images. A program referring to the constitutive relation of materials involving high temperature were written, integrating the strain and temperature field to obtain the stress evolution during the welding process and residual stress field.

3 Result and discussion

The ROI strain map along axis x (parallel to the axis of weld) and y (perpendicular to x) at 15 s after the arc is showed in Fig. 6a, b, respectively. The displacement and the strain values of each subset in the ROI can be calculated by solving the first-order shape function with the highest correlation between the current and the reference subsets as follows:

$$x' = \mathrm{x} + u_0 + \frac{\partial u}{\partial x}dx + \frac{\partial u}{\partial y}dy \tag{1}$$

$$y' = \mathrm{y} + v_0 + \frac{\partial v}{\partial x}dx + \frac{\partial v}{\partial y}dy \tag{2}$$

where (x, y) is the coordinate of the reference subset's center, (x', y') is the center of the subset after deformation, and u_0 and v_0 are the subset's displacements in direction x and y, respectively. The 2D-DIC strain measurement ignored the out-of-plane displacement, but the strain due to the out-of-plane motion has been reduced by increasing the object distance over 1 m [24], reducing the error down to the magnitude of 10^{-6}. Correlation between the current and reference subsets can be calculated by solving one of the commonly used correlation criteria as follows [25]:

$$C_{cc} = \frac{\sum_{(i,j)\in S}\left(f\left(x_{ref_i}, y_{ref_j}\right)-f_m\right)\left(g\left(x_{cur_i}, y_{cur_j}\right)-g_m\right)}{\sqrt{\sum_{(i,j)\in S}\left[\left(f\left(x_{ref_i}, y_{ref_j}\right)-f_m\right)\right]^2 \sum_{(i,j)\in S}\left[\left(g\left(x_{cur_i}, y_{cur_j}\right)-g_m\right)\right]^2}} \tag{3}$$

$$C_{LS} = \sum_{(i,j)\in S}\left[\frac{f\left(x_{ref_i}, y_{ref_j}\right)-f_m}{\sqrt{\sum_{(i,j)\in S}\left[\left(f\left(x_{ref_i}, y_{ref_j}\right)-f_m\right)\right]^2}} - \frac{g\left(x_{cur_i}, y_{cur_j}\right)-g_m}{\sqrt{\sum_{(i,j)\in S}\left[\left(g\left(x_{cur_i}, y_{cur_j}\right)-g_m\right)\right]^2}}\right]^2 \tag{4}$$

where S represents a subset, (x_{ref}, y_{ref}) and (x_{cur}, y_{cur}) are coordinates in a reference subset and corresponding deformed current subset, respectively. f and g are the reference and current image functions, respectively, and return a grayscale value corresponding to the specified (x, y) point. f_m and g_m are the mean grayscale values of the reference and current subset, respectively. It can be seen that the matching results (i.e., correlation) of the reference and current subset are related to the gray value of the images, and the result varies due to the changes of the gray value of the current image. An area with a width of about 5 mm near the fusion line was oxidized during the welding process. Changes of the gray value in this area would affect the matching result. Therefore, the ROI showed in Fig. 6 was not included in this area. In order to further improve the matching accuracy, noise reduction and luminance balance were applied to the images of the speckle pattern region before the strain was calculated. Figure 6a shows the longitudinal (along x-axis) strain map of the ROI during the welding process. When the torch is passing, the strain along the axis x is negative with the longitudinal shrinkage underneath a GTAW torch. The transverse (along axis y) strain field developed after welding (Fig. 6b) could be due to the following two factors: first, the base metal moved outwards from the weld center owing to thermal expansion of the weld. Second, compressive plastic deformation was developed in base metal around the weld pool when the arc reached. During cooling, it shrinks toward the axis of the weld and dragged base metal to the negative direction of y. In

combination with the two factors above, a positive displacement was accrued in the zone near the weld because the expansion was greater than the shrink. Meanwhile, a negative displacement was accrued in the zone far from the weld because the expansion was smaller than the shrink.

Figure 7a–b shows the longitudinal strain evolution of P1 ~ P3 corresponding to the points in the hole-drilling method in experiments I and II, respectively. Figure 7c–d shows the transverse strain evolution of P1 ~ P3 in experiments I and II, respectively. The peak of strain evolution in each direction as well as temperature (showed in Fig. 7e–f) in P2 appeared earlier than P1 and P3 since the arc first past through P2.

The linearized stepwise increment method is mainly used for analyzing the nonlinear relationship of material [26]. The whole load is divided into a certain amount of parts and acts on the structure gradually. A stress increment $\Delta\delta$ and a strain increment $\Delta\varepsilon$ come into being once a load is added on a structure with stress and strain; it can be considered that the relationship between $\Delta\delta$ and $\Delta\varepsilon$ is linear when the increment is small enough, and the calculation of stress is infinitely close to the actual status. The instruction of solving nonlinear problems with a linearized stepwise increment method in one degree of freedom is showed in Fig. 8. The thermal-dependent relationship between $\Delta\delta$ and $\Delta\varepsilon$ in incremental theory are as follows:

$$\Delta\delta = D_e(\Delta\varepsilon - \Delta\varepsilon_0) \tag{5}$$

$$\Delta\delta = D_{ep}(\Delta\varepsilon - \Delta\varepsilon_0) + \Delta\sigma_0 \tag{6}$$

where D_e is the elastic matrix, D_{ep} is the plastic matrix, and $\Delta\sigma_0$ represents the stress increment due to temperature change, all these three are related to material's thermal and mechanical properties; $\Delta\varepsilon$ is the total strain; and $\Delta\varepsilon_0$ is the strain increment owing to temperature increment. After inferring the strain steps from the strain evolution and corresponding temperature steps from temperature data, $\Delta\delta$ can be calculated with the formulas (5) and (6) in elastic and plastic sections with
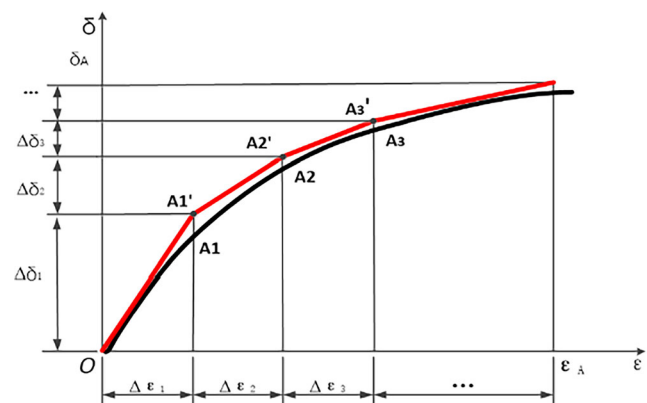

Fig. 8 Linearized stepwise increment method

thermophysical and mechanical properties of the base metal, respectively. Since plane stress is a good assumption for a welded plate with a 6-mm thickness, the current study assumed out-of-plane stress is 0.

The stress computation flowchart is showed in Fig. 9. The temperature during welding changed dramatically when the arc past, causing large strain value with a magnitude of $10^{-3} \sim 10^{-4}$ in a short period of time (acquisition interval is 0.2 s). According to the linearized stepwise increment method,

a great strain increment step might result in great stress measurement error. The stress increment error would propagate because D_{ep} is concerned with the current stress status. In order to diminish the error, efforts were made when designing the stress calculation algorithm whose flowchart is shown in Fig. 9. The temperature and strain increment exceeding a certain threshold were divided equally into small parts. The case of reverse loading was separated out to calculate in a different way. This approach reduced the error to some extent, but the
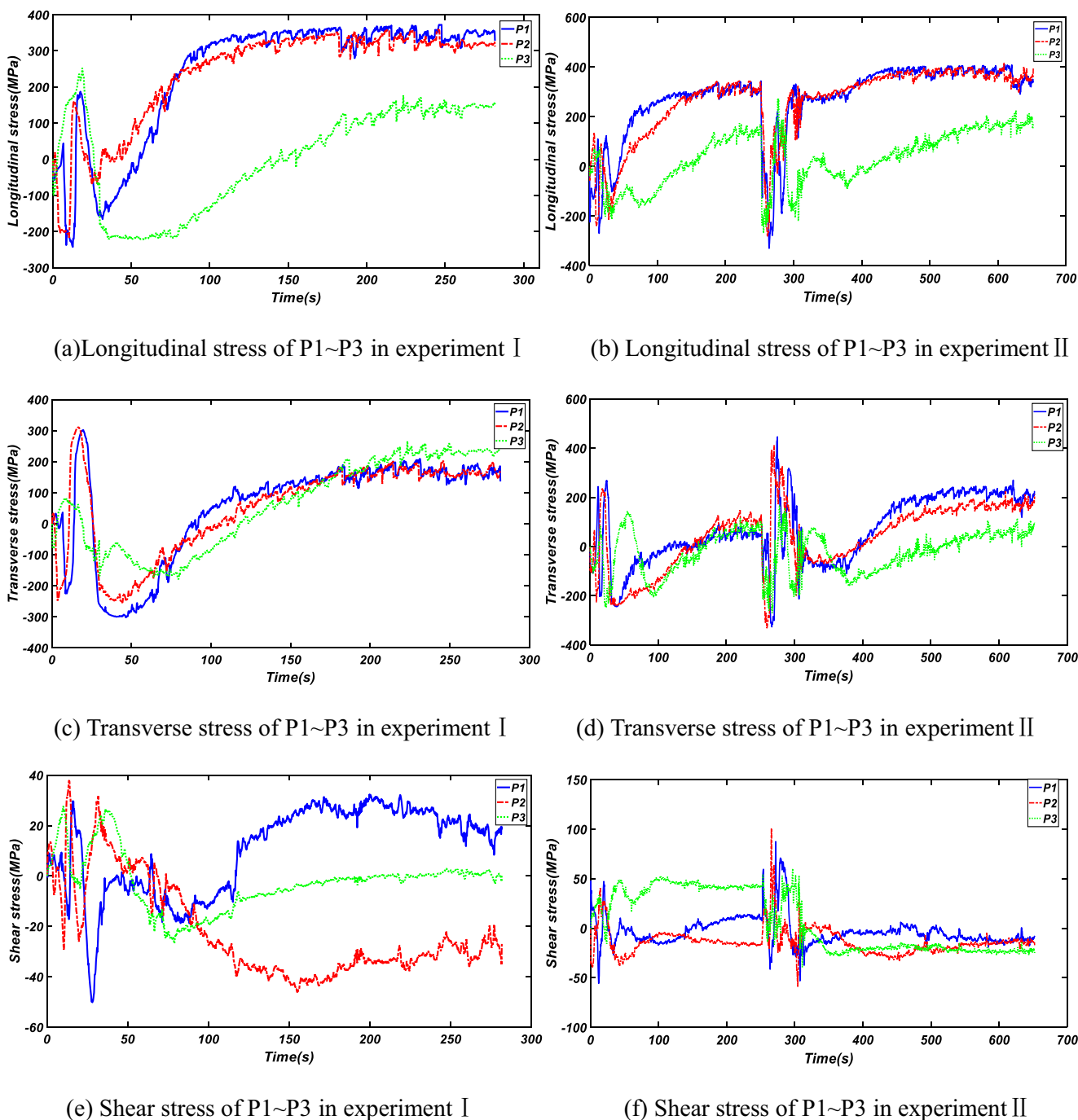

(a) Longitudinal stress of P1~P3 in experiment Ⅰ

(b) Longitudinal stress of P1~P3 in experiment Ⅱ

(c) Transverse stress of P1~P3 in experiment Ⅰ

(d) Transverse stress of P1~P3 in experiment Ⅱ

(e) Shear stress of P1~P3 in experiment Ⅰ

(f) Shear stress of P1~P3 in experiment Ⅱ

Fig. 9 Flowchart of stress computation algorithm

equalization process did not match a smaller strain increment with a corresponding temperature increment accurately. An error could be further minimized by increasing the image acquisition FPS and frequency of temperature sampling to obtain a smaller and more accurate increment correspondence.

The longitudinal stress evolution of P1 ~ P3 in experiments I and II is showed in Fig. 10a, b, respectively, where positive values indicate tensile stress and negative values indicate

compressive stress. After filling the first layer in both of the experiments, the longitudinal residual stress at P1 and P2 were almost the same and it is greater than P3 which was farther from the weld. The transverse stress evolution in experiments I and II are showed in Fig. 10c, d. After the first welding process in both of the experiments, the transverse residual stress at P3 was greater than P1, which implied that the residual stress of the point farther from the weld was greater than
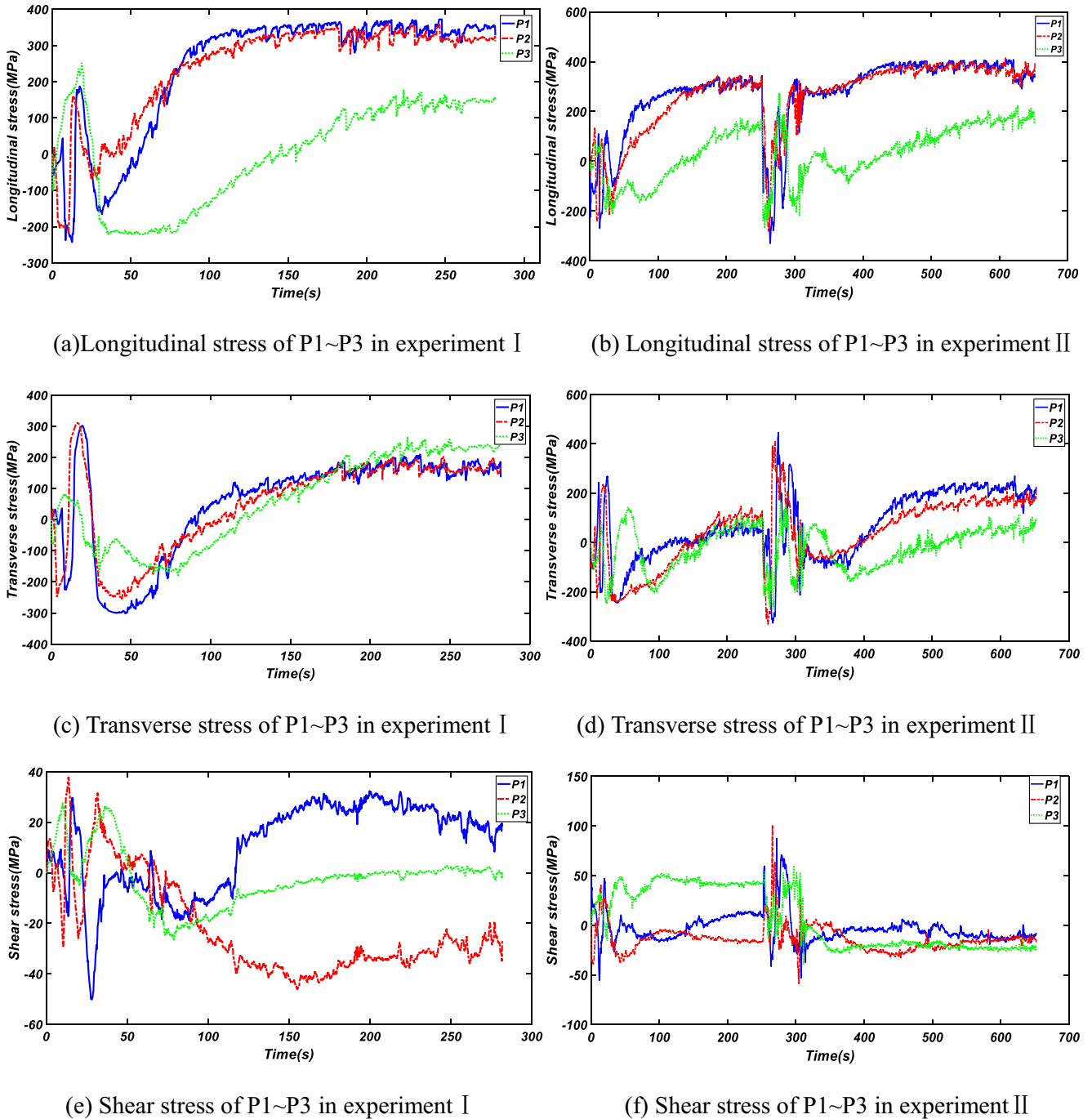

(a) Longitudinal stress of P1~P3 in experiment I

(b) Longitudinal stress of P1~P3 in experiment II

(c) Transverse stress of P1~P3 in experiment I

(d) Transverse stress of P1~P3 in experiment II

(e) Shear stress of P1~P3 in experiment I

(f) Shear stress of P1~P3 in experiment II

Fig. 10 The stress evolution of P1 ~ P3 in experiments I and II. **a** Longitudinal stress evolution of P1 ~ P3 in experiment I. **b** Longitudinal stress evolution of P1 ~ P3 in experiment II. **c** Transverse stress evolution of P1 ~ P3 in experiment I. **d** Transverse stress evolution of P1 ~ P3 in experiment II. **e** Shear stress evolution of P1 ~ P3 in experiment I. **f** Shear stress evolution of P1 ~ P3 in experiment II
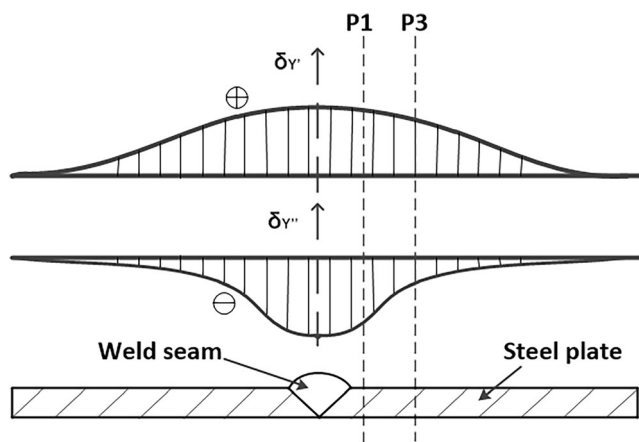
Fig. 11 Residual stress component distribution on cross-section in transverse

the nearer one. It differs from the traditional residual stress distribution. The transverse residual stress distribution of butt welding consists of two parts: first, tensile stress spread in the middle of the plates and compressive stress in both ends due to the shrink of the weld, the tensile residual stress distribution of the cross-section in the middle is showed in Fig. 11($\sigma_{y'}$). Second, contrary to the above, compressive stress spread in the middle and tensile stress in both ends because that the first weld processed hinders the subsequent from shrinking in the transverse, the compressive residual stress distribution of the cross-section in the middle is showed in Fig. 11($\sigma_{y''}$). The fact that the compressive stress at P3 was much smaller than that at P1 might result in the consequence that the transverse

Fig. 12 The residual stress map in experiments I and II. **a** Longitudinal residual stress map (experimentI). **b** Longitudinal residual stress map (experiment II). **c** Transverse residual stress map (experiment I). **d** Transverse residual stress map (experiment II). **e** Shear residual stress map (experiment I). **f** Shear residual stress map (experiment II)

(a) Longitudinal residual stress map (experiment I)

(b) Longitudinal residual stress map (experiment II)

(c) Transverse residual stress map (experiment I)

(d) Transverse residual stress map (experiment II)

(e) Shear residual stress map (experiment I)

(f) Shear residual stress map (experiment II)
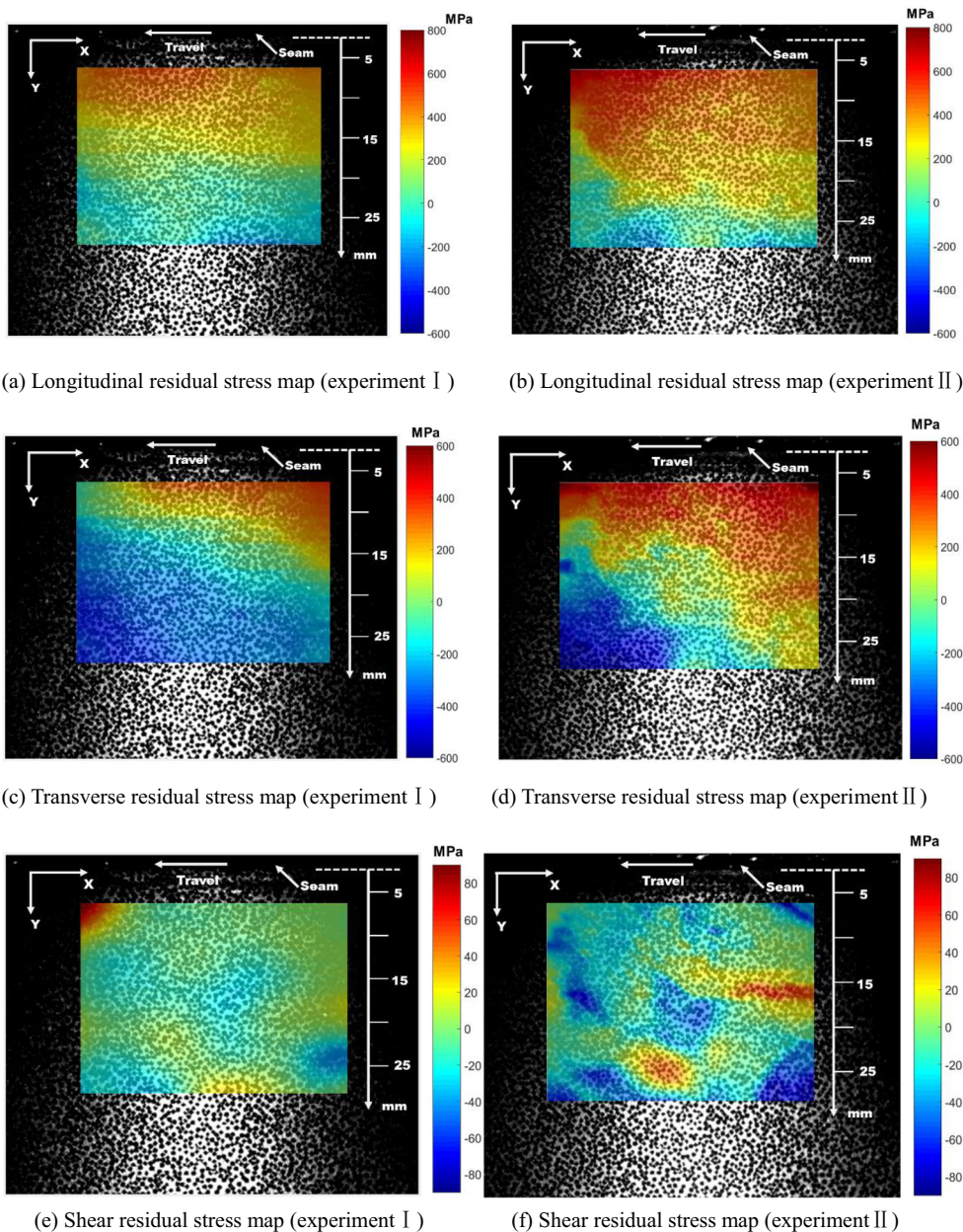
residual stress at P3 was greater than P1. Figure 10e, f shows the shear stress evolution of P1 ~ P3 in both of the experiments.

The longitudinal, transverse, and shear residual stress map of ROI in experiments I and II are showed in Fig. 12a–f. The longitudinal residual stress of the region with the same distance from the weld is in the same level, and the stress varied from tensile to compressive from the weld center toward HAZ. The tensile transverse residual stress region where the weld was manufactured first was larger than the subsequent ones. Residual stress in all of the three directions intensified after the second weld procedure, and the tensile residual stress region was broadened.

Figure 13a, b shows the comparison of the residual stress of P1 ~ P3 measured with the two different methods in experiments I and II. In experiment I, the largest difference between the two methods appeared in the longitudinal stress of P1 and the shear stress of P2 with a value of 24 MPa, and the remaining were similar.

In experiment II, the largest difference appeared in the transverse stress of P3 with a value of 37 MPa. The difference in experiment II was greater than that in experiment I. The difference is due to the fact that images were taken at ~2 s after the welding arc was on and large strain appeared within 2 s resulted in stress increment error as discussed above. Furthermore, in experiment II, residual stress error in the final is intensified due to the residual stress after the first welding pass.

4 Conclusions

High-temperature stress evolution measurement and residual stress measurement based on 2D-DIC were used to study the mechanical behavior of 304 stainless steel plates during TIG welding process. Based on the investigation, the following conclusions can be made:

Fig. 13 Residual stress measured with different methods in experiments I and II. **a** Residual stress (experiment I). **b** Residual stress (experiment II)
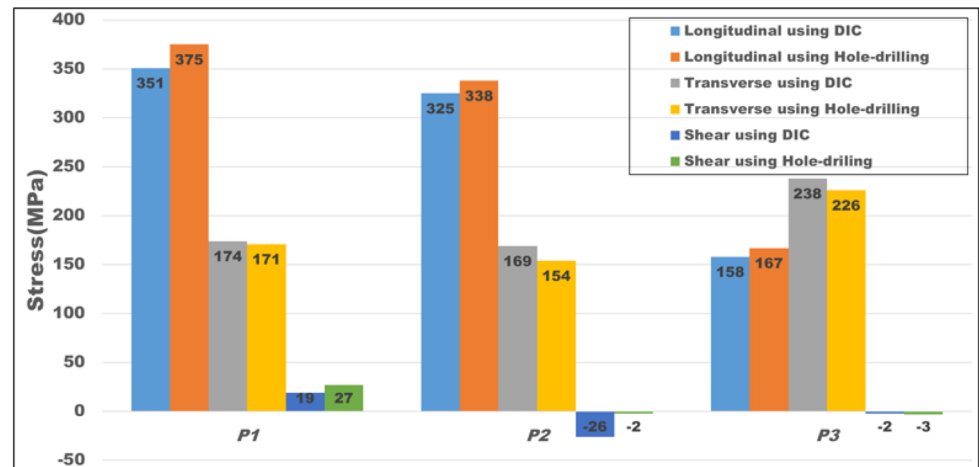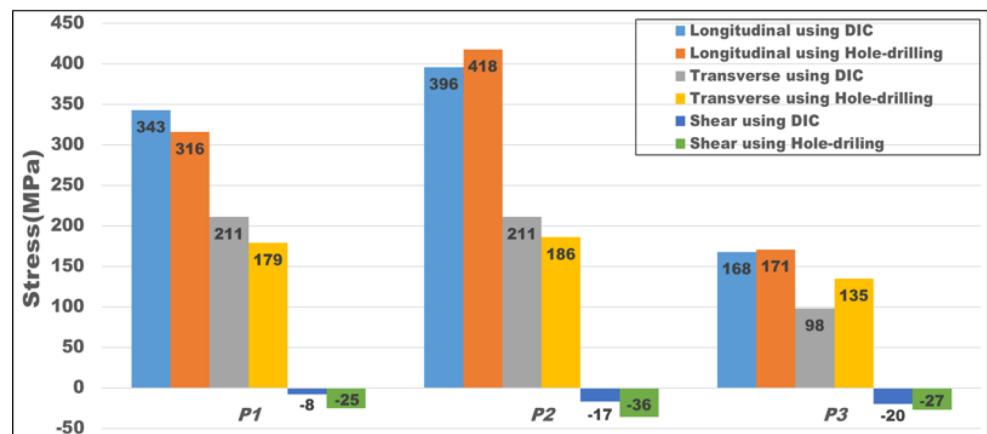
(1) A new full-field residual stress and high-temperature stress evolution measurement method were developed by integrating a stress increment calculation program, a full-field strain calculation, a special optical illumination and filtering system, and a novel surface high-temperature resistant speckle preparation.

(2) The validation result shows that the new non-destructive residual stress technique agrees with the stress measured by the hole-drilling method.

(3) Stress evolution could be obtained and be further used for adjusting welding procedures to achieve lower tensile residual stress in the weld.

(4) Measurement error analysis was performed, and several possible approaches were proposed to diminish the residual stress measurement error in the new technique.

References

1. Withers PJ, Bhadeshia HKDH (2001) Residual stress. Part 2—nature and origins. Mater Sci Technol 17(4):366–375
2. De A, DebRoy T (2011) A perspective on residual stresses in welding. Sci Technol Weld Join 16(3):204–208
3. Dong P (2005) Residual stresses and distortions in welded structures: a perspective for engineering applications. Sci Technol Weld Join 10(4):389–398
4. Deplus K, Simar A, Haver WV, Meester BD (2011) Residual stresses in aluminum alloy friction stir welds. Int J Adv Manuf Technol 56:493–504
5. Feng Z (2005) Processes and mechanisms of welding residual stress and distortion. Woodhead Publishing, Cambridge
6. Rossini NS, Dassisti M, Benyounis KY (2012) Methods of measuring residual stresses in components. Mater Des 35:572–588
7. Younis NT, Kang B (2011) Averaging effects of a strain gage. J Mech Sci Technol 25(1):163–169
8. Baldi A (2014) Residual stress measurement using hole drilling and integrated digital image correlation techniques. Exp Mech 54(3):379–391
9. Nelson DV, Makino A, Schmidt T (2006) Residual stress determination using hole drilling and 3D image correlation. Exp Mech 46(1):31–38
10. Gao J, Shang H (2009) Deformation-pattern-based digital image correlation method and its application to residual stress measurement. Appl Opt 48(7):1371–1381
11. Rangaswamy P, Griffith ML, Prime MB, Holden TM, Rogge RB, Edwards JM, Sebring RJ (2005) Residual stresses in LENS components using neutron diffraction and contour method. Mater Sci Eng A 399(1–2):72–83
12. Ganguly S, Stelmukh V, Edwards L, Fitzptrick ME (2008) Analysis of residual stress in metal-inert-gas-welded Al-2024 using neutron and synchrotron X-ray diffraction. Mater Sci Eng A 491(1–2):248–257
13. Acevedo C, Evans A, Nussbaumer A (2012) Neutron diffraction investigations on residual stresses contributing to the fatigue crack growth in ferritic steel tubular bridges. Int J Pres Ves Pip 95(7):31–38
14. Prime MB, Thomas G-H, Baumann JA, Lederich RJ, Bowden DM, Sebring R (2006) Residual stress measurements in a thick, dissimilar aluminum alloy friction stir weld. Acta Mater 54(15):4013–4021
15. Pan B, Qian K, Xie H, Asundi A (2009) Two-dimensional digital image correlation for in-plane displacement and strain measurement: a review. Meas Sci Technol 20(6):1–17
16. Jae B (2019) Completely in situ and non-contact warpage assessment using 3D DIC with virtual patterning method. Int J Adv Manuf Technol 100:2803–2811
17. Hild F, Roux S (2006) Digital image correlation: from displacement measurement to identification of elastic properties – a review. Strain 42(2):69–80
18. Li ZG, He N, Fan ZM, Liao HL (2013) The study of non-contact measure method for deformation based on the digital image correlation. Adv Mater Technol 718-720:853–857
19. Li GY, Xu FX, Sun GY, Li Q (2014) Identification of mechanical properties of the weld line by combining 3D digital image correlation with inverse modeling procedure. Int J Adv Manuf Technol 74:893–905
20. Henry TC, Phillips FR, Cole DP, Garboczi E, Haynes RA, Johnson T (2020) In situ fatigue monitoring investigation of additively manufactured maraging steel. Int J Adv Manuf Technol 107:3499–3510
21. Agarwal G, Gao H, Amirthalingam M, Hermans MJM (2018) In situ strain investigation during laser welding using digital image correlation and finite-element-based numerical simulation. Sci Technol Weld Join 23(2):134–139
22. Chen J, Feng Z (2018) Strain and distortion monitoring during arc welding by 3D digital image correlation. Sci Technol Weld Join 23(6):536–542
23. Chen J, Yu XH, Miller RG, Feng Z (2014) In situ strain and temperature measurement and modelling during arc welding. Sci. Technol. Weld Joining 20(3):181–188
24. Sutton MA, Yan JH, Tiwari V, Schreier HW, Orteu JJ (2008) The effect of out-of-plane motion on 2D and 3D digital image correlation measurements. Opt Lasers Eng 46(10):746–757
25. Blaber J, Adair B, Antoniou A (2015) Ncorr: open-source 2D digital image correlation Matlab software. Exp Mech 55(6):1105–1122
26. Liu ZX (2010) Computational solid mechanics. China, Shanghai Jiao Tong University Publishing, Shanghai